Cosmogenic-neutron activation of TeO_2 and implications for neutrinoless double-β decay experiments

B. S. Wang,[1] E. B. Norman,[1,2] N. D. Scielzo,[2] A. R. Smith,[3] K. J. Thomas,[1,3] and S. A. Wender[4]
[1]*Department of Nuclear Engineering, University of California, Berkeley, California 94720, USA*
[2]*Lawrence Livermore National Laboratory, Livermore, California 94550, USA*
[3]*Lawrence Berkeley National Laboratory, Berkeley, California 94720, USA*
[4]*Los Alamos National Laboratory, Los Alamos, New Mexico 87545, USA*
(Received 27 February 2015; published 27 August 2015)

Flux-averaged cross sections for cosmogenic-neutron activation of natural tellurium were measured using a neutron beam containing neutrons of kinetic energies up to ∼800 MeV and having an energy spectrum similar to that of cosmic-ray neutrons at sea level. Analysis of the radioisotopes produced reveals that ^{110m}Ag will be a dominant contributor to the cosmogenic-activation background in experiments searching for neutrinoless double-β decay of ^{130}Te, such as the Cryogenic Underground Observatory for Rare Events (CUORE) and the Sudbury Neutrino Observatory Plus (SNO+). An estimate of the cosmogenic-activation background in the CUORE experiment has been obtained using the results of this measurement and cross-section measurements of proton activation of tellurium. Additionally, the measured cross sections in this work are also compared with results from semiempirical cross-section calculations.

DOI: 10.1103/PhysRevC.92.024620 PACS number(s): 25.40.Sc, 29.30.Kv, 29.25.Dz, 23.40.−s

I. INTRODUCTION

Neutrinoless double-β ($0\nu\beta\beta$) decay [1–3] is a long-sought-after second-order weak process in which a nucleus (A,Z) transitions to a nucleus $(A,Z+2)$ through the emission of two electrons. This process is hypothesized to occur only if neutrinos are Majorana particles. Observation of $0\nu\beta\beta$ decay would not only establish that neutrinos are Majorana fermions but also may constrain the neutrino-mass scale and hierarchy and demonstrate that total lepton number is not conserved.

In experiments searching for $0\nu\beta\beta$ decay, the signature of interest is a peak at the double-β decay Q value ($Q_{\beta\beta}$). As $0\nu\beta\beta$ decay would be a rare process, minimizing the background rate around $Q_{\beta\beta}$ is essential for improving the experimental sensitivity. Therefore, a detailed characterization of all potential sources of background is important, as any event that can mimic or obscure the $0\nu\beta\beta$-decay peak is problematic, must be well understood, and, if possible, eliminated.

To minimize external backgrounds, $0\nu\beta\beta$-decay experiments operate in underground laboratories, where large overburdens decrease the flux of cosmic rays by orders of magnitude relative to the flux above ground [4]. Further reduction of the remaining cosmic-ray background can be achieved with muon-veto detectors, and backgrounds from natural radioactivity in the laboratory environment can be alleviated with proper shielding.

Radioactivity present within the detector itself can provide a source of background that is difficult to eliminate. $0\nu\beta\beta$-decay experiments devote a great deal of effort into making ultraclean and ultrapure detector materials free of primordial radioisotopes. However, no matter how clean or purely produced the materials are, cosmogenic activation will generate some radioactivity while the materials are at or above the Earth's surface during storage, production, or transportation [5–7]. The background contribution from this radioactivity can be minimized by ensuring detector materials spend as little time above ground as possible and by avoiding air transportation, as the cosmic-ray flux increases significantly at higher altitudes [8,9]. At sea level, activation is primarily caused by the hadronic component of the cosmic-ray flux, which is dominated by neutrons [10].

This work investigates the backgrounds associated with cosmogenic activation of tellurium, which are important to understand for experiments such as the Cryogenic Underground Observatory for Rare Events (CUORE) [11] and the Sudbury Neutrino Observatory Plus (SNO+) [12] that are searching for the $0\nu\beta\beta$ decay of ^{130}Te, but to date are poorly characterized due to a lack of data. As $0\nu\beta\beta$-decay experiments run for several years, typically only long-lived cosmogenic isotopes (i.e., that have half-lives on the order of a year or longer) with Q values near or greater than the ^{130}Te $Q_{\beta\beta}$ of 2528 keV [13–16] will be potential sources of background at the $0\nu\beta\beta$-decay peak.

Determining the resulting cosmogenic-activation background contribution to a $0\nu\beta\beta$-decay experiment requires estimating the production rates of the radioisotopes in tellurium. Activation cross sections that span a wide range of neutron energies, from thermal up to several GeV, are therefore needed; however, experimentally measured cross-section data are currently sparse. For neutron energies above 800 MeV, cross sections for neutron activation are expected to be approximately equal to those for proton activation due to the energy of the incident particle being much higher than the ∼10-MeV Coulomb potential between a proton and a tellurium nucleus. Neutron-activation cross sections at such energies can be estimated from existing experimental data taken for protons between 800 MeV and tens of GeV [17–19]. In these proton measurements, two long-lived radioisotopes were observed that have the potential to contribute background at the $0\nu\beta\beta$-decay peak: ^{110m}Ag and ^{60}Co. Below 800 MeV, experimental data exist for activation of natural tellurium by ∼1−180 MeV neutrons [20] and activation of individual

tellurium isotopes by thermal to ∼15-MeV neutrons [21]; however, only a few reactions were measured, and no cross sections were reported for the production of ^{60}Co and ^{110m}Ag. To deal with the lack of experimental data, the background from cosmogenic activation has been estimated in the past (as in Ref. [7]) using a combination of the aforementioned neutron and proton measurements and codes that either implement the semiempirical formulas by Silberberg and Tsao (S&T) [22–24] (e.g., YIELDX [22–24], ACTIVIA [25]) or are based on Monte Carlo (MC) methods (e.g., CEM03 [26], HMS-ALICE [27], GEANT4 [28,29]).

These estimates can be greatly improved with additional neutron-activation cross-section measurements below 800 MeV, which can also be used to benchmark the S&T and MC codes. A sample of natural-TeO_2 powder was irradiated at the Los Alamos Neutron Science Center (LANSCE) with a neutron beam containing neutrons with kinetic energies up to ∼800 MeV, and having an energy distribution that resembles the cosmic-ray neutron flux at sea level. Following exposure, the γ rays emitted from the sample were measured in a low-background environment with a high-purity-germanium (HPGe) detector to determine the radioisotopes present. Based on these results, flux-averaged cross sections were obtained for several dozen isotopes.

The cross sections are used to investigate the impact cosmogenic activation will have on CUORE, a next-generation $0\nu\beta\beta$-decay experiment that will use an array of 988 high-resolution, low-background natural-TeO_2 bolometers to search for the $0\nu\beta\beta$ decay of ^{130}Te. In addition, the measured cross sections are compared with cross sections calculated using the ACTIVIA code. Details of this measurement and subsequent analysis are discussed below.

II. EXPERIMENTAL METHOD AND DATA ANALYSIS

A. Target

The target consisted of 272 g of natural-TeO_2 powder held within a cylindrical plastic container wrapped on all sides with 0.05 cm of cadmium to remove thermal neutrons. The front and back cadmium layers were also used to monitor the neutron flux on either side of the target. Circular aluminum and gold foils were placed throughout the target to monitor the neutron flux as well. The target geometry is illustrated in Fig. 1, and the details of each target component are listed in Table I.

B. Neutron irradiation

The target was irradiated with neutrons from the LANSCE 30R beam line for 43 h during February 25–27, 2012. At LANSCE, neutrons are generated from spallation reactions induced by an 800-MeV pulsed proton beam incident on a tungsten target. The 30R beam line, which is 30° to the right of the proton beam, has a neutron-energy spectrum that closely resembles the cosmic-ray neutron spectrum at sea level, but has an intensity 3×10^8 times larger, as shown in Fig. 2. A beam collimation width of 8.26 cm was used, which resulted in a beam-spot diameter of 8.41 cm at the target.

The proton beam used to generate the neutrons consisted of 625-μs-long macropulses occurring at a rate of 40 Hz.

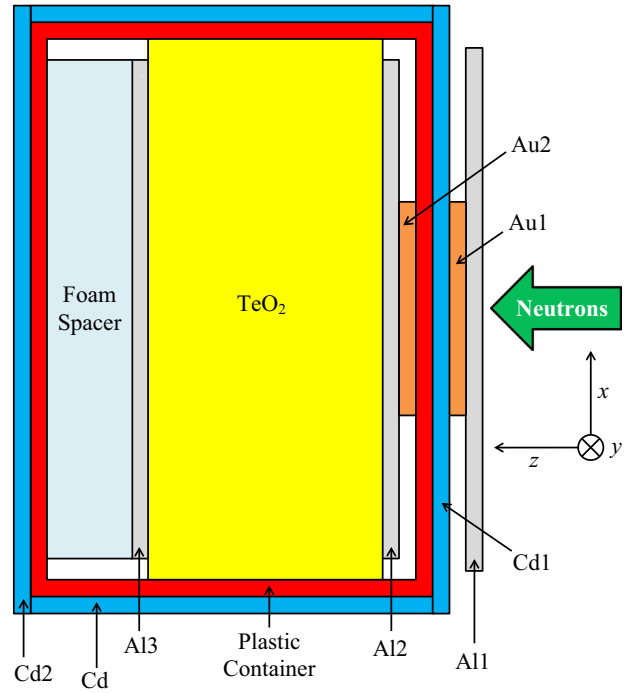

FIG. 1. (Color online) Schematic of the target irradiated at LANSCE. The entire target is 6.2 cm long in the z direction. Each target component has cylindrical symmetry about the z axis. This drawing is not to scale. Details on each component are given in Table I.

Each macropulse contained micropulses spaced 1.8 μs apart. The neutron time of flight was obtained by measuring the time between the arrival of the proton macropulse at the tungsten target and the generation of a fission signal in a ^{238}U-fission ionization chamber [32] located 25.4 cm upstream of the TeO_2 target. The ionization chamber was only able to detect neutrons with energies above the ^{238}U-fission threshold, which is approximately 1.25 MeV. The average neutron flux above 1.25 MeV at the TeO_2 target was determined to be 1.41×10^6 $(\text{cm}^2\text{s})^{-1}$, with an estimated uncertainty of 10% [33] based on uncertainties in the geometry and efficiency of the ionization chamber.

C. γ-ray analysis of the irradiated target

Approximately one week after the neutron irradiation, the TeO_2 target was dismantled, and each component was analyzed using γ-ray spectroscopy at the Lawrence Berkeley National Laboratory Low Background Facility [34,35]. The TeO_2 powder, cadmium foils, and aluminum foils were measured using an upright, 115%-relative-efficiency, n-type HPGe detector, and the gold foils were measured with a horizontal, 80%-relative-efficiency, p-type HPGe detector. Each detector was surrounded by a copper inner shield encased in a lead outer shield. The gold foils were highly activated and could be counted at a distance of 12 cm from the detector. The cadmium and aluminum foils had low levels of activity and were therefore measured directly on top of the detector to maximize the detection efficiency. For the TeO_2 powder, the γ-ray measurements needed to be highly sensitive to

TABLE I. Description of the target components illustrated in Fig. 1. The material, dimensions, mass, and purpose of each component are given. The parameters Δz and d are the thickness of the component along the z axis and the diameter in the x-y plane, respectively.

Component	Material	Δz (cm)	d (cm)	Mass (g)	Purpose
TeO_2	TeO_2 powder	2.79	6.43	271.56	Target
Al1	Al	0.0813	6.22	6.68	Neutron-flux monitor
Al2	Al	0.0813	5.93	6.06	Neutron-flux monitor
Al3	Al	0.0813	5.93	6.06	Neutron-flux monitor
Au1	Au	0.00515	2.54	0.504	Neutron-flux monitor
Au2	Au	0.00512	2.54	0.500	Neutron-flux monitor
Cd1	Cd	0.05	6.7	16.3	Neutron-flux monitor Thermal-neutron absorber
Cd2	Cd	0.05	7.3	19.9	Neutron-flux monitor Thermal-neutron absorber
Cd	Cd	0.05			Thermal-neutron absorber
Plastic Container	Polystyrene	0.2			Target holder

long-lived radioisotopes, which had low levels of activity inside the powder. To maximize the detection efficiency, the TeO_2 powder was mixed thoroughly and counted in a Marinelli beaker positioned over the top of the detector (Fig. 3). A plastic insert was placed inside the beaker to decrease the thickness and increase the height of the powder, which in turn increased the solid angle of the detector seen by the powder and decreased the self-attenuation of γ rays from decays within the powder. The thickness and average height of the TeO_2 powder were 3.8 mm and ~5.6 cm, respectively. The TeO_2 was counted in this configuration periodically for ~3 years to enable the observation of long-lived activation products after the short-lived ones decayed away. Figure 4 shows a γ-ray spectrum for the TeO_2 powder collected four months after the irradiation.

Each peak in the γ-ray spectra was fit with a Gaussian summed with a quadratic background function to determine the energy and net counts. For peaks with higher intensity, a smoothed step function was also added to the fitting function. The γ-ray energies were used to identify the radioisotopes produced in the TeO_2 powder. For γ-ray lines that could come from the decay of more than one isotope, the contributors were identified from the decay half-life of the line.

A list of the radioisotopes observed in the TeO_2 powder is provided in Table II. Since γ-ray measurements started one week after the neutron irradiation ended, only activated isotopes with half-lives greater than ~1 day remained. Therefore, any observed isotope with a shorter half-life was a decay daughter of a longer-lived isotope. For example, the presence of ^{127}Te (9.35-h half-life) and ^{129}Te (69.6-min half-life) was due to the decays of the longer-lived metastable states ^{127m}Te and ^{129m}Te, respectively.

D. Photopeak efficiencies

The γ-ray measurements of the TeO_2 powder needed to be highly sensitive to long-lived radioisotopes, which had low levels of activity inside the powder. To maximize the detection efficiency, the powder was counted immediately next to the detector (Fig. 3). Determination of the photopeak efficiencies (i.e., probability that the γ ray of interest will

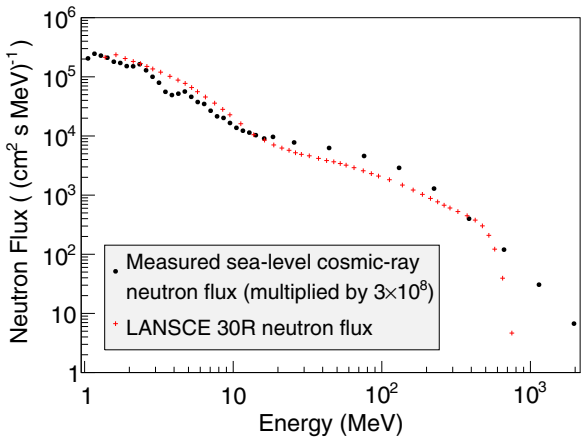

FIG. 2. (Color online) LANSCE 30R neutron flux (red [gray]) [30] compared with the measured sea-level cosmic-ray-neutron flux (black) [31].

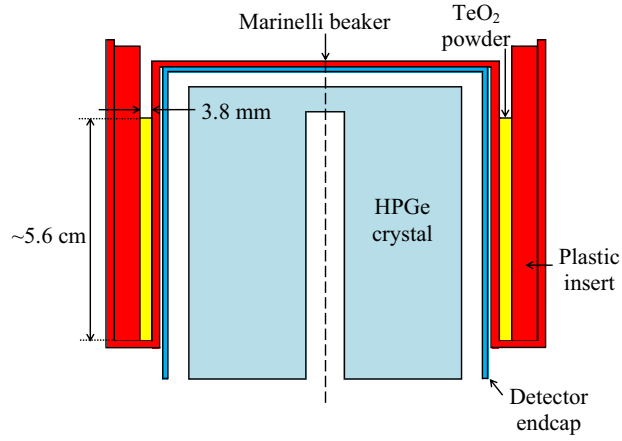

FIG. 3. (Color online) Setup used during the γ-ray measurement of the TeO_2 powder. Each component has cylindrical symmetry about the dashed line. This drawing is not to scale.

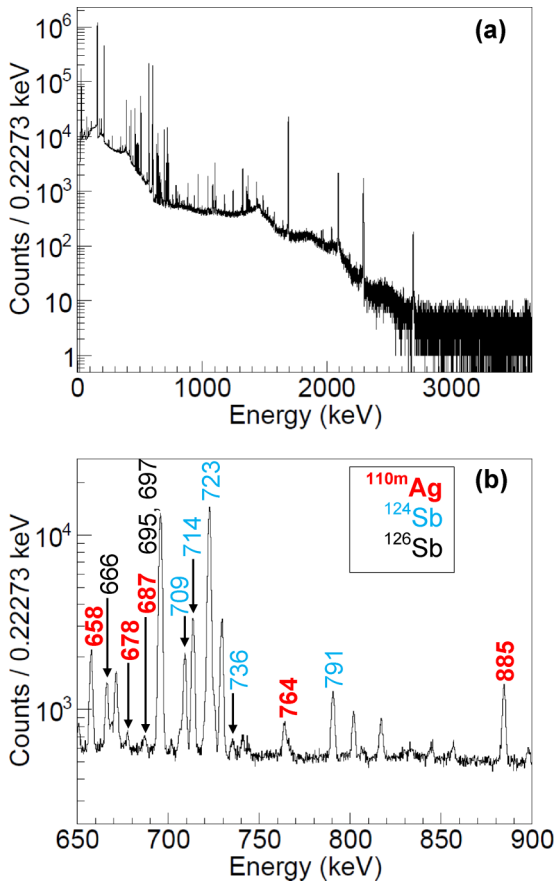

FIG. 4. (Color online) Three-day-long γ-ray spectrum collected for the TeO_2 powder four months after the neutron irradiation. (a) Full spectrum. (b) A region of the spectrum where ^{110m}Ag peaks were observed. Labeled peaks are associated with the decay of isotopes with Q values greater than the $Q_{\beta\beta}$ of ^{130}Te, i.e., ^{110m}Ag (red [gray] and bolded), ^{124}Sb (blue [gray]), and ^{126}Sb (black). Other peaks in the region are from the decays of ^{125}Sb, ^{129m}Te, ^{105}Ag, and ^{114m}In.

deposit its *full* energy in the detector) for the TeO_2 powder from calibration measurements alone was impractical due to the complexity of the counting geometry and the effects of true-coincidence summing, which can be significant at such close range. Therefore, the efficiencies were obtained by running simulations with the GEOMETRY AND TRACKING 4 (GEANT4) code, version 4.9.4.p02, which were benchmarked against experimental measurements of various point and extended γ-ray sources (Table III) that covered a wide range of γ-ray energies.

For the benchmarking measurements, the ^{57}Co and ^{54}Mn point sources were each counted at the center of the detector face and at four positions along the side of the detector that were spaced 2 cm apart and spanned the length of the HPGe crystal. The uranium source was counted on the side of the detector as well. Following the natural-source method [36], the two extended sources, ES1 and ES2, were constructed from powders that contained elements with naturally occurring long-lived radioisotopes. ES1 was designed to mimic the geometry of the irradiated TeO_2 powder during the γ-ray measurements, and ES2 was designed to mimic both the geometry and density of the powder.

Photopeak efficiencies were obtained for all the γ rays listed in Table III. In addition, the total efficiency (i.e., probability that the γ ray of interest will deposit *any amount* of energy above threshold in the detector) was obtained for the two ^{57}Co γ rays (122.06 and 136.47 keV) and the ^{54}Mn γ ray (834.85 keV).

The benchmarking measurements were simulated using GEANT4. Each simulation included the HPGe detector, the γ-ray source, and the lead and copper shielding. For each γ ray of interest, the entire decay scheme of the parent nucleus was simulated. Angular correlations between coincident γ rays were not taken into account; however, at close distances to the detector, the effects on the photopeak efficiencies are largely averaged out and are thus small.

Each simulated photopeak or total efficiency ($\epsilon_{s\gamma}$) was compared with the measured value ($\epsilon_{m\gamma}$), and the percent difference was determined:

$$\Delta\epsilon_\gamma = \frac{\epsilon_{m\gamma} - \epsilon_{s\gamma}}{\epsilon_{s\gamma}} \times 100\%. \quad (1)$$

Using the manufacturer's detector specifications in the simulations resulted in $\Delta\epsilon_\gamma$ values that ranged from approximately -10% to -35%, with the agreement between simulation and measurement worsening at lower γ-ray energies. This kind of disagreement, especially overestimation by the simulation, has been seen in other studies that model the γ-ray efficiencies of HPGe detectors using the geometry provided by the manufacturer (e.g., Refs. [37–40]). Typically, the discrepancies have been attributed to physical characteristics of the detector (crystal location, Li-diffused-contact thickness, etc.) that are difficult for the manufacturer to precisely specify. When the source is counted close to the detector, small uncertainties in the detector's parameters can have significant effects on the γ-ray efficiencies.

The larger disagreement at low energies between the simulated and measured efficiencies pointed to additional, unspecified attenuating material that was present in the actual detector. To address this, the thickness of the aluminum mounting cup that immediately surrounds the HPGe crystal was increased by 2.25 mm to achieve closer agreement between the simulations and measurements. Discrepancies were also present when calibration sources were placed along the side of the detector, near the bottom of the HPGe crystal ($\sim$8 cm below the top of the detector endcap). To investigate this issue in detail, the detected count rate of 59.5-keV γ rays from a collimated ^{241}Am source was measured along the side of the detector. A drop-off in the intensity of the 59.5-keV line was observed before where one would expect, given the nominal length of the crystal. This effect could be due either to the crystal being shorter than the nominal length or to the presence of attenuating material not specified by the manufacturer. Simulations were carried out for both possibilities. Shortening the crystal to 80.5 mm or keeping the nominal crystal length and adding a 1.85-mm-thick, 3.5-cm-long copper ring around the aluminum mounting cup, 8 cm below the top of the detector endcap, both provided good agreement with the benchmarking measurements. Since the results of each case were effectively equivalent and the presence of a ring around the bottom of

TABLE II. Radioisotopes observed in the irradiated TeO_2 powder. Unless otherwise indicated, all isotopes were produced by neutron interactions with tellurium. The measured and calculated flux-averaged cross sections ($\bar{\sigma}_{30R}$ and $\bar{\sigma}_{S\&T}$, respectively) for neutron activation of tellurium are provided for isotopes with half-lives greater than 1 day. All $\bar{\sigma}_{30R}$ were measured at the 68% confidence level (C.L.) and are independent cross sections, except for those followed by "(cu)," which are cumulative. All rows corresponding to isotopes that can contribute background at the ^{130}Te $0\nu\beta\beta$-decay peak are bolded, and for these isotopes, the decay modes (ϵ and β^- for electron capture and β-minus decay, respectively) and Q values are given.

Isotope	Half-life	$\bar{\sigma}_{30R}$(68% C.L.) (mb)	$\bar{\sigma}_{S\&T}$ (mb)	Decay Q value (MeV)
^{126}I[a]	12.93 d			
^{131}I[a]	8.025 d			
^{118}Te	6.00 d	5.7 ± 1.2	9.80	
^{119m}Te	**4.7 d**	**6.3 ± 0.8**	**13.0**	**2.554 (ϵ)**
^{121}Te[b]	19.17 d			
^{121m}Te	164.2 d	16 ± 2	25.2	
^{123m}Te	119.2 d	36 ± 4	8.6	
^{125m}Te	57.4 d	83 ± 10	17.0	
^{127}Te	9.35 h			
^{127m}Te	106.1 d	46 ± 9	25.3	
^{129}Te	69.6 min			
^{129m}Te	33.6 d	53 ± 17 (cu)	22.4 (cu)	
^{131}Te	25 min			
^{131m}Te[b]	33.25 h			
^{131m}Xe[a]	11.84 d			
^{118}Sb	**3.6 min**			**3.657 (ϵ)**
^{119}Sb[c]	38.19 h			
^{120m}Sb	**5.76 d**	**6.3 ± 0.8**	**10.2**	**2.681 + E_{ex} (ϵ)**
^{122}Sb	2.7238 d	14 ± 2 (cu)	15.4 (cu)	
^{124}Sb	**60.2 d**	**16 ± 2 (cu)**	**19.1 (cu)**	**2.904 (β^-)**
^{125}Sb	2.759 yr	18 ± 2 (cu)	18.8 (cu)	
^{126}Sb	**12.35 d**	**6.7 ± 0.9 (cu)**	**26.4 (cu)**	**3.673 (β^-)**
^{127}Sb	3.85 d	13 ± 2 (cu)	9.8 (cu)	
^{113}Sn	115.1 d	2.6 ± 0.3 (cu)	3.0 (cu)	
^{117m}Sn	14 d	4.3 ± 0.6	0.63	
^{111}In	2.805 d	2.3 ± 0.3 (cu)	2.1 (cu)	
^{114m}In	49.51 d	1.9 ± 0.2	0.31	
^{105}Ag	41.29 d	0.56 ± 0.07 (cu)	0.45 (cu)	
^{106m}Ag	**8.28 d**	**0.44 ± 0.09**	**0.39**	**3.055 (ϵ)**
^{110}Ag	**24.56 s**			**2.893 (β^-)**
^{110m}Ag	**249.83 d**	**0.28 ± 0.04**	**0.054**	**3.010 (β^-)**
^{111}Ag	7.45 d	0.42 ± 0.09 (cu)	0.030 (cu)	
^{101}Rh	3.3 yr	0.06 ± 0.01 (cu)	0.24 (cu)	
^{101m}Rh	4.34 d	0.30 ± 0.05 (cu)	0.24 (cu)	
^{102m}Rh	3.742 yr	0.15 ± 0.02	0.12	
^{60}Co[d]	**5.27 yr**	**<0.0016 (cu)**	**0.0013 (cu)**	**2.823 (β^-)**
^{7}Be[e]	53.24 d	1.4 ± 0.2	2.5	

[a]This isotope was produced by interactions with spallation protons created in the target during the neutron irradiation. Therefore, no cross sections are provided.

[b]This isotope had a high probability of being produced by interactions with <1.25-MeV neutrons. Therefore, no cross sections are given.

[c]A flux-averaged cross section could not be obtained for ^{119}Sb because the strongest γ-ray line at 24 keV overlapped with x-rays emitted by other activated isotopes.

[d]^{60}Co was not conclusively observed in the γ-ray spectra due to ^{102m}Rh and ^{110m}Ag peaks being present where the ^{60}Co peaks were expected. Therefore the cross section quoted for ^{60}Co is an upper limit.

[e]^{7}Be was produced almost exclusively by neutron interactions with oxygen. The cross sections given correspond to these interactions.

the crystal was unknown, the simulated efficiencies for the 80.5-mm-long crystal were used in the cross-section analysis.

The adjustments listed in Table IV were applied to the detector geometry in GEANT4 to make the efficiencies from the simulations more closely match those from the benchmarking measurements. Figure 5 shows the resulting values of $\Delta\epsilon_\gamma$. The uncertainties in $\Delta\epsilon_\gamma$ take into account the statistical uncertainties in the measurements and the simulations, as well as the uncertainties in the source activities and branching ratios of the γ rays. The total uncertainty in the simulated

TABLE III. Description of γ-ray sources used to benchmark GEANT4.

Source	Composition	Dimensions	γ-ray (keV)	Branching Ratio(%)
Co-57	Co-57	Point source	122.06	85.60 ± 0.17
			136.47	10.68 ± 0.08
Mn-54	Mn-54	Point source	834.85	99.9760 ± 0.0010
Uranium[a]	Natural uranium ore (0.1176 g)	Diameter = 4.76 cm	185.72 (^{235}U)	57.2 ± 0.8
	mixed with epoxy	Thickness = 3.175 mm	46.54 (^{210}Pb)	4.25 ± 0.04
			186.21 (^{226}Ra)	3.64 ± 0.04
			242.00 (^{214}Pb)	7.251 ± 0.016
			295.22 (^{214}Pb)	18.42 ± 0.04
			1764.49 (^{214}Bi)	15.30 ± 0.03
			2204.06 (^{214}Bi)	4.924 ± 0.018
ES1[b]	La_2O_3 powder (89 g),	Inner radius = 5.06 cm	201.83 (^{176}Lu)	78.0 ± 2.5
	Lu_2O_3 powder (2 g),	Outer radius = 5.443 cm	306.78 (^{176}Lu)	93.6 ± 1.7
	KCl powder (4 g)	Average height = 5.75 cm	788.74 (^{138}La)	34.4 ± 0.5
			1435.80 (^{138}La)	65.6 ± 0.5
			1460.82 (^{40}K)	10.66 ± 0.18
			269.46 (^{223}Ra)	13.9 ± 0.3
			271.23 (^{219}Rn)	10.8 ± 0.6
			832.01 (^{211}Pb)	3.52 ± 0.06
			351.07 (^{211}Bi)	13.02 ± 0.12
ES2[b]	(Unirradiated) TeO_2 powder (228 g),	Inner radius = 5.06 cm	Note: All γ rays used	
	La_2O_3 powder (23 g),	Outer radius = 5.443 cm	to analyze ES1 were also	
	Lu_2O_3 powder (6 g),	Average height = 6.5 cm	used to analyze ES2.	
	K_2SO_4 powder (14 g)			

[a]All isotopes in the source were assumed to be in secular equilibrium.
[b]Due to a small ^{227}Ac contamination in the La_2O_3, ES1 and ES2 also contained ^{227}Ac and its daughter isotopes, which were assumed to be in secular equilibrium with each other. γ rays from the ^{227}Ac chain are also listed in the table.

efficiencies was estimated to be 5%, which is slightly larger than the standard deviation of $\Delta\epsilon_\gamma$. It should be noted that, with the exception of the photopeak efficiencies for the 201.83- and 306.78-keV γ rays from ^{176}Lu decay, all other photopeak and total efficiencies in Fig. 5 are either not affected or negligibly affected by true coincidence summing. The 201.83- and 306.78-keV γ rays, on the other hand, have a high probability of being emitted in cascade with each other and with an 88.34-keV γ ray, and therefore both are affected by summing. The fact that photopeak and total efficiencies with little or no summing effects and photopeak efficiencies with summing effects can be obtained from the simulations with 5% uncertainty gives confidence that summing can also be modeled adequately for the present cross-section analysis.

The photopeak efficiencies of the γ rays used to identify the isotopes in Table II were obtained for the irradiated TeO_2 powder by performing GEANT4 simulations using the adjusted detector values in Table IV. Simulations indicate that summing could have as much as a 40% effect for certain photopeak efficiencies. Figure 5 gives confidence that the GEANT4 simulations could provide photopeak efficiencies for the irradiated TeO_2 powder with around 5% uncertainty.

E. Neutron attenuation in the TeO_2 powder

During irradiation, the neutron flux within the TeO_2 powder was not uniform due to neutron attenuation through the material. For each isotope in Table II, this attenuation would result in an average isotope-production rate in the powder that is a fraction, $\bar{T}$, of the rate one would expect without attenuation. To estimate $\bar{T}$, the levels of activation in the aluminum and cadmium foils located in front of and behind the powder (see Fig. 1) were compared. The ratio, $\bar{T}_b$, of activity in the back foils (Al3, Cd2) relative to that in the

TABLE IV. Detector parameters adjusted in the GEANT4 simulations. The nominal values provided by the manufacturer are given, along with the values that allowed for satisfactory (∼5%) agreement between the efficiencies from the simulations and the benchmarking measurements.

Parameter	Nominal value (mm)	Adjusted value (mm)
Length of HPGe crystal	85.5	80.5[a]
Distance between HPGe crystal and detector window	0	2
Thickness of aluminum mounting cup	0.5	2.75
Thickness of internal dead layer (lithium contact)	1	2

[a]As explained in Sec. II D, shortening the crystal to 80.5 mm, or keeping the nominal crystal length and adding a 1.85-mm-thick, 3.5-cm-long copper ring around the aluminum mounting cup, 8 cm below the top of the detector endcap, provided good agreement with the benchmarking measurements. Since the results of each case were effectively equivalent and the presence of a ring around the bottom of the crystal was unknown, the simulated efficiencies for the 80.5-mm-long crystal were used in the cross-section analysis.

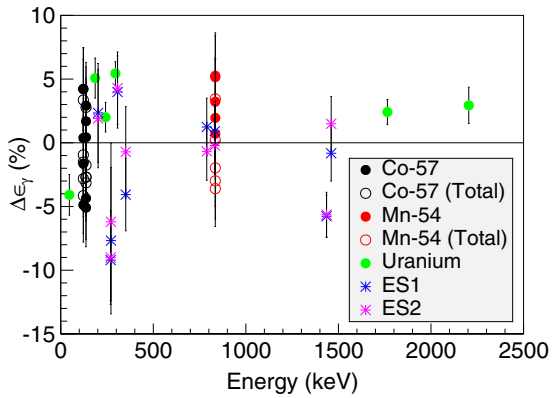

FIG. 5. (Color online) Percent differences between the measured and simulated γ-ray efficiencies as a function of γ-ray energy. The simulated efficiencies were obtained using the adjusted values in Table IV. Points corresponding to total efficiencies are indicated with "(Total)" in the legend. All other points correspond to photopeak efficiencies.

front foils (Al1, Cd1) provides a measure of the effect of neutron attenuation through the entire TeO_2 powder. $\bar{T}$ can then be simply estimated as the average of the effects at the front and back of the powder; specifically, if one assumes that neutrons participating in isotope production have little attenuation through the target components upstream of the powder, $\bar{T} \simeq (1 + \bar{T}_b)/2$. Table V gives the values of $\bar{T}_b$ determined for the production of ^{22}Na, ^{105}Ag, and ^{110m}Ag in the foils. The spread in the results can be attributed to the neutron-energy dependence of the attenuation.

The value of $\bar{T}$ for an isotope is affected by the energy dependence of the isotope-production cross section. For the isotopes in Table II, the energy dependences are mostly unknown for the full neutron-energy range of interest. However, the production threshold energies for the isotopes cover a range similar to that for the reactions listed in Table V (i.e., a few MeV for $Cd(n,X)^{105}Ag$ and $Cd(n,X)^{110m}Ag$ to tens of MeV for $^{27}Al(n,X)^{22}Na$). Because of this similarity in threshold energies and the effects of neutron attenuation being reasonably small, $\bar{T}_b$ for all isotopes was taken to be 0.90 ± 0.10, which encompasses the values given in Table V along with their uncertainties. Therefore, a value of $\bar{T} = 0.95 \pm 0.05$ was used for all the isotopes considered in this work.

TABLE V. Neutron attenuation through the TeO_2 powder. Column one lists radioisotope-production reactions that occurred in the aluminum and cadmium foils located in front of and behind the TeO_2 powder during the neutron irradiation. For each reaction, the ratio, $\bar{T}_b$, of the activity in the back foil relative to that in the front foil is given. Uncertainties quoted are statistical.

Reaction	$\bar{T}_b$
$^{27}Al(n,X)^{22}Na$	0.98 ± 0.03
$Cd\ (n,X)^{105}Ag$	0.84 ± 0.01
$Cd\ (n,X)^{110m}Ag$	0.86 ± 0.01

F. Isotope-production rates

The production rate for each isotope can be determined from the γ-ray spectra collected for the irradiated TeO_2 powder during the 3-year period following the neutron irradiation. In most cases, the isotope produced in the powder either is not fed by other isotopes during and after the irradiation, or is fed by isotopes with much shorter half-lives. Under either condition, the production rate, R_{30R}, can be obtained using

$$R_{30R} = \frac{\lambda C_\gamma}{B_\gamma \epsilon_\gamma [\exp(-\lambda t_s) - \exp(-\lambda t_e)][1 - \exp(-\lambda t_{\rm irrad})]}, \tag{2}$$

where λ is the decay constant of the isotope, C_γ is the number of counts in the γ-ray peak of interest, B_γ is the branching ratio of the γ ray, ϵ_γ is the photopeak efficiency of detecting the γ ray (discussed in Sec. II D), $t_{\rm irrad}$ is the neutron-irradiation time, and t_s and t_e are respectively the start time and end time of the γ-ray measurement relative to the end of the irradiation. The production rates for ^{125m}Te and ^{127m}Te were described by more complex growth-and-decay relations and were obtained using the appropriate modifications to Eq. (2).

For each isotope, the branching ratio and decay constant were taken from the National Nuclear Data Center NuDat 2.6 online database [41]. The number of counts in the γ-ray line of interest was monitored over time to confirm it exhibited the expected decay behavior, and the γ-ray measurement that provided the best statistics for C_γ was then used to determine the isotope-production rate. When obtaining the isotope-production cross sections, uncertainties in C_γ, B_γ, λ, and ϵ_γ were taken into account; however, for most of the isotopes, the 10% uncertainty in the LANSCE neutron flux dominates the uncertainty in the cross section.

G. Flux-averaged cross sections

The flux-averaged cross section, $\bar{\sigma}_{30R}$, for neutron activating an isotope in the irradiated TeO_2 powder is determined from

$$\bar{\sigma}_{30R} = \frac{\int_{E_{\rm min}}^{E_{\rm max}} \sigma(E)\varphi_{30R}(E)dE}{\int_{E_{\rm min}}^{E_{\rm max}} \varphi_{30R}(E)dE}, \tag{3}$$

where $\sigma(E)$ is the cross section for producing the isotope with neutrons of kinetic energy E, $\varphi_{30R}(E)$ is the differential neutron flux hitting the front of the target in units of [(cm^2 s MeV)$^{-1}$], and $E_{\rm min}$ and $E_{\rm max}$ are respectively the lowest and highest neutron energies hitting the TeO_2 powder.

The isotope-production rate can also be expressed as

$$R_{30R} \approx N\bar{\sigma}_{30R}\bar{T}\int_{E_{\rm min}}^{E_{\rm max}} \varphi_{30R}(E)dE, \tag{4}$$

where N is the number of tellurium nuclei in the powder (except for the production of ^{7}Be, where N is the number of oxygen nuclei in the powder). The parameter $\bar{T}$ is included to account for the attenuation of the neutron beam through the TeO_2 powder during irradiation.

The ^{238}U-fission ionization chamber at LANSCE was only able to detect neutrons with energies >1.25 MeV. The total neutron flux below 1.25 MeV during the irradiation was

determined to be non-negligible based on the amount of ^{198}Au created by (n,γ) reactions in the gold foils. Therefore, cross sections could be obtained only for isotopes produced solely (or primarily) by interactions with neutrons of energy >1.25 MeV. For isotopes with production threshold energies >1.25 MeV, $E_{\rm min}$ and $E_{\rm max}$ from Eq. (4) could safely be set to 1.25 and 800 MeV, respectively. In Table II, cross sections are also provided for metastable tellurium isotopes, which could in principle be produced by (n,γ) and (n,n') reactions with neutrons of energy <1.25 MeV. However, at low neutron energies, these reactions are not expected to contribute significantly to the production of metastable states because the nuclear spins of the states are $\geqslant 5$ higher than those of the stable tellurium nuclei. We therefore determine cross sections for these isotopes by assuming that neutrons below 1.25 MeV do not impart enough angular momentum to populate a metastable state.

The flux-averaged cross sections, shown in Table II, are determined from Eqs. (2) and (4). In Table II, independent cross sections are those that include only direct production of the isotope; cumulative cross sections are those that include both direct and indirect production of the isotope.

III. COMPARING MEASURED AND CALCULATED CROSS SECTIONS

Isotope-production cross sections for tellurium were also obtained by using the ACTIVIA code to perform calculations based on the S&T semiempirical formulas. These formulas were originally developed to describe proton-nucleus interactions, but they are assumed to be applicable to neutron-nucleus interactions as well. The calculated cross sections are reported in Table II. Although the formulas are only valid for proton and neutron energies $\geqslant 100$ MeV and they do not distinguish between ground and metastable states in product nuclei, the calculated and measured cross sections agree reasonably well, within a factor of 3 on average. One should note that the cross section calculated for ^{110m}Ag was underestimated by approximately a factor of 5.

IV. COSMOGENIC-ACTIVATION BACKGROUND IN THE CUORE EXPERIMENT

The CUORE experiment, currently being constructed at the Gran Sasso National Laboratory (LNGS), will use an array of 988 high-resolution, low-background TeO_2 bolometers to search for the $0\nu\beta\beta$ decay of ^{130}Te. Each bolometer is composed of a $5\times5\times5$ cm^3 natural-TeO_2 crystal that serves as both a source and a detector of the decay. CUORE is aiming for a background rate of 10^{-2} counts/(keV kg yr) at the ^{130}Te $Q_{\beta\beta}$ value of 2528 keV, which would allow the experiment to reach a half-life sensitivity of 9.5×10^{25} years (90% confidence level), assuming a live time of 5 years and a full-width-at-half-maximum energy resolution of 5 keV [42].

Using the results of the neutron-activation measurement discussed in this work and the proton-activation measurements of Ref. [19], one can determine the background contribution to CUORE from the cosmogenic activation of the TeO_2 crystals that occurs during sea transportation from the crystal-production site in Shanghai, China to LNGS in Italy. The results of both this work and Ref. [19] indicate that ^{110m}Ag and ^{60}Co are the only two long-lived radioisotopes that will contribute meaningfully to the background at the $0\nu\beta\beta$-decay peak due to their Q values being greater than $Q_{\beta\beta}$. ^{110}Ag will also contribute a small amount to the background because ^{110m}Ag decays to it 1.33% of the time.

The production rates, R, of ^{110m}Ag and ^{60}Co were each estimated to be

$$R \approx N \sum_i \sigma_i \phi_{{\rm CR},i}, \tag{5}$$

where σ_i is the isotope-production cross section assigned to energy bin i, and $\phi_{{\rm CR},i}$ is the differential cosmic-ray neutron flux at sea level integrated over energy bin i. The energy bins, integrated fluxes, and σ_i values are given in Table VI. The cosmic-ray neutron flux determined by Gordon *et al.* [31] was used in this analysis, with the parameter $F_{\rm BSYD}$ from Ref. [31] taken to be 0.73 ± 0.22 [33] for the route used to ship the TeO_2 crystals. 80% of the ^{110m}Ag and as much as 37% of the ^{60}Co were produced by 1.25–800 MeV neutrons.

The fraction of ^{110m}Ag, ^{110}Ag, and ^{60}Co decays that deposit energy in a 60-keV-wide region of interest (ROI) surrounding the $0\nu\beta\beta$-decay peak was estimated using GEANT4 simulations of a single $5\times5\times5$ cm^3 TeO_2 crystal. The values obtained were 0.5%, 0.4%, and 1% for ^{110m}Ag, ^{110}Ag, and ^{60}Co decays, respectively. In the full CUORE array, the presence of nearby crystals would often lead to energy being deposited in more than one crystal. As most $0\nu\beta\beta$ decays would deposit all of their energy in a single crystal, the background can be reduced by rejecting events in which energy was deposited in more than one crystal. Simulations of a $3\times3\times3$ TeO_2-crystal array indicate that rejecting multicrystal events can suppress the ^{110m}Ag contribution to the ROI by a factor of ~2, while the contributions from ^{110}Ag and ^{60}Co will be minimally affected.

To estimate the background rate at $Q_{\beta\beta}$ from cosmogenic activation of TeO_2, the following assumptions were made: (1) each crystal spends 3 months at sea level, (2) no ^{110m}Ag, ^{110}Ag, and ^{60}Co were present at the beginning of shipment due to their removal during the crystal-growth process, and (3) crystals were delivered to LNGS and stored underground at a constant rate from early 2009 to late 2013 [33]. The resulting contamination levels for ^{110m}Ag + ^{110}Ag and ^{60}Co when CUORE begins operation in late 2015 will be $\sim2\times10^{-8}$ Bq/kg and $\sim10^{-9}$ Bq/kg, respectively, which correspond to background rates of $\sim6\times10^{-5}$ counts/(keV kg yr) and $\sim7\times10^{-6}$ counts/(keV kg yr), respectively. After 5 years of running, the contamination levels will decrease to $\sim2\times10^{-10}$ Bq/kg for ^{110m}Ag+^{110}Ag and $\sim6\times10^{-10}$ Bq/kg for ^{60}Co, which correspond to background rates of $\sim4\times10^{-7}$ counts/(keV kg yr) and $\sim4\times10^{-6}$ counts/(keV kg yr), respectively. The contamination levels given here are lower than those predicted in Ref. [7] due to Lozza *et al.* assuming a longer exposure time of 1 year and a shorter overall cooling time underground of 2 years. Rejecting multisite events should decrease the ^{110m}Ag+^{110}Ag background rates by a factor of ~2. Although the background rates in the ROI are at least two orders of magnitude lower than the current CUORE goal background of 10^{-2} counts/(keV kg yr), for future experiments striving for

TABLE VI. Energy bins used in the estimation of the ^{110m}Ag and ^{60}Co production rates. The differential cosmic-ray neutron flux at sea level integrated over each bin is provided. The isotope-production cross sections assigned to each bin are also listed. For bin 1, the cross sections obtained in this work are used. For bins 2, 3, and 4, the cross sections used were those measured in proton-activation experiments with 800 MeV, 1.4 GeV, and 23 GeV protons respectively. The individual contributions to R in units of (s^{-1}) and (%) are given in the last two columns.

Bin	Bin range	Integrated neutron flux ($(cm^2\ s)^{-1}$)	Cross section (mb)		Contribution to R (s^{-1})	
			^{110m}Ag	^{60}Co	^{110m}Ag	^{60}Co
1	1.25–800 MeV	$(3.7 \pm 1.3) \times 10^{-3}$	0.28 ± 0.04	<0.0016	$(2.9 \pm 1.1) \times 10^{-6}$ (80%)	$<(1.7 \pm 0.6) \times 10^{-8}$ (<37%)
2	800 MeV to 1.4 GeV	$(5.3 \pm 1.9) \times 10^{-5}$	3.95 ± 0.40 [a] [43]	0.09 ± 0.04 [19]	$(5.9 \pm 2.2) \times 10^{-7}$ (16%)	$(1.4 \pm 0.8) \times 10^{-8}$ (>30%)
3	1.4–23 GeV	$(2.6 \pm 1.0) \times 10^{-5}$	1.9 ± 0.3 [19]	0.20 ± 0.04 [19]	$(1.4 \pm 0.6) \times 10^{-7}$ (3.9%)	$(1.5 \pm 0.6) \times 10^{-8}$ (>33%)
4	23–150 GeV	$(1.6 \pm 0.6) \times 10^{-7}$	0.88 ± 0.59 [19]	0.75 ± 0.08 [19]	$(4.0 \pm 3.1) \times 10^{-10}$ (0.01%)	$(3.4 \pm 1.3) \times 10^{-10}$ (>0.8%)

[a]The value of this cross section was reported incorrectly in Ref. [19] but correctly in Ref. [43].

essentially zero background, cosmogenic activation may have to be addressed more stringently.

V. CONCLUSIONS

Flux-averaged cross sections for cosmogenic-neutron activation of radioisotopes in natural tellurium were measured by irradiating TeO_2 powder with a neutron beam containing neutrons of kinetic energies up to ~800 MeV, and having an energy spectrum similar to that of cosmic-ray neutrons at sea level. The cross sections obtained for ^{110m}Ag and ^{60}Co, the two isotopes which have both half-lives of order a year or longer and Q values larger than the $Q_{\beta\beta}$ of ^{130}Te, were combined with results from tellurium activation measurements with 800 MeV to 23 GeV protons to estimate the background in the CUORE experiment from cosmogenic activation of the TeO_2 crystals. The anticipated ^{110m}Ag+^{110}Ag and ^{60}Co background rates in [counts/(keV kg yr)] at the $0\nu\beta\beta$-decay peak were determined to be $\sim 6 \times 10^{-5}$ and $\sim 7 \times 10^{-6}$, respectively, at the beginning of counting and $\sim 4 \times 10^{-7}$ and $\sim 4 \times 10^{-6}$, respectively, after 5 years of counting. The ^{110m}Ag+^{110}Ag rates should decrease by a factor of ~2 if multicrystal events are efficiently rejected. These rates are at least two orders of magnitude lower than the goal background for the CUORE experiment.

ACKNOWLEDGMENTS

We gratefully acknowledge the many valuable discussions with Maura Pavan and Silvia Capelli from the CUORE Collaboration. This work was supported by Lawrence Livermore National Laboratory under Contract No. DE-AC52-07NA27344, Los Alamos National Laboratory under Contract No. DE-AC52-06NA25396, Lawrence Berkeley National Laboratory under Contract No. DE-AC02-05CH11231, the U.S. Department of Energy Office of Defense Nuclear Nonproliferation (NA-22), the U.S. Department of Energy National Nuclear Security Administration under Award No. DE-NA0000979, and the Nuclear Forensics Graduate Fellowship from the U.S. Department of Homeland Security under Grant Award No. 2012-DN-130-NF0001-02. The views and conclusions contained in this document are those of the authors and should not be interpreted as necessarily representing the official policies, either expressed or implied, of the U.S. Department of Homeland Security.

[1] F. T. Avignone III, S. R. Elliot, and J. Engel, Rev. Mod. Phys. **80**, 481 (2008).
[2] W. Rodejohann, Int. J. Mod. Phys. E **20**, 1833 (2011).
[3] S. M. Bilenky and C. Giunti, Mod. Phys. Lett. A **27**, 1230015 (2012).
[4] M. Aglietta, B. Alpat, E. D. Alyea, P. Antonioli, G. Badino, G. Bari, M. Basile, V. S. Berezinsky, F. Bersani, M. Bertaina, R. Bertoni, G. Bonoli, A. Bosco, G. Bruni, G. Cara Romeo, C. Castagnoli, A. Castellina, A. Chiavassa, J. A. Chinellato, L. Cifarelli, F. Cindolo, G. Conforto, A. Contin, V. L. Dadykin, A. De Silva, M. Deutsch, P. Dominici, L. G. Dos Santos, L. Emaldi, R. I. Enikeev, F. L. Fabbri, W. Fulgione, P. Galeotti, C. Ghetti, P. Ghia, P. Giusti, R. Granella, F. Grianti, G. Guidi, E. S. Hafen, P. Haridas, G. Iacobucci, N. Inoue, E. Kemp, F. F. Khalchukov, E. V. Korolkova, P. V. Korchaguin, V. B. Korchaguin, V. A. Kudryavtsev, K. Lau, M. Luvisetto, G. Maccarone, A. S. Malguin, R. Mantovani, T. Massam, B. Mayes, A. Megna, C. Melagrana, N. Mengotti Silva, C. Morello, J. Moromisato, R. Nania, G. Navarra, L. Panaro, L. Periale, A. Pesci, P. Picchi, L. Pinsky, I. A. Pless, J. Pyrlik, V. G. Ryasny, O. G. Ryazhskaya, O. Saavedra, K. Saitoh, S. Santini, G. Sartorelli, M. Selvi, N. Taborgna, V. P. Talochkin, J. Tang, G. C. Trinchero, S. Tsuji, A. Turtelli, I. Uman, P. Vallania, G. Van Buren, S. Vernetto, F. Vetrano, C. Vigorito, E. von Goeler, L. Votano, T. Wada, R. Weinstein, M. Widgoff, V. F. Yakushev, I. Yamamoto, G. T. Zatsepin, and A. Zichichi, Phys. Rev. D **58**, 092005 (1998).
[5] S. Cebrián, J. Amaré, B. Beltrán, J. M. Carmona, E. García, H. Gómez, I. G. Irastorza, G. Luzón, M. Martínez, J. Morales,

A. O. D. Solórzano, C. Pobes, J. Puimedón, A. Rodríguez, J. Ruz, M. L. Sarsa, L. Torres, and J. A. Villar, J. Phys.: Conf. Series **39**, 344 (2006).
[6] S. R. Elliott, V. E. Guiseppe, B. H. LaRoque, R. A. Johnson, and S. G. Mashnik, Phys. Rev. C **82**, 054610 (2010).
[7] V. Lozza and J. Petzoldt, Astropart. Phys. **61**, 62 (2015).
[8] W. N. Hess, H. Wade Patterson, and R. Wallace, Phys. Rev. **116**, 445 (1959).
[9] P. Goldhagen, J. M. Clem, and J. W. Wilson, Radiat. Prot. Dosim. **110**, 387 (2004).
[10] G. Heusser, Annu. Rev. Nucl. Part. Sci. **45**, 543 (1995).
[11] C. Arnaboldi, F. Avignone III, J. Beeman, M. Barucci, M. Balata, C. Brofferio, C. Bucci, S. Cebrian, R. Creswick, S. Capelli, L. Carbone, O. Cremonesi, A. de Ward, E. Fiorini, H. Farach, G. Frossati, A. Giuliani, D. Giugni, P. Gorla, E. Haller, I. Irastorza, R. McDonald, A. Morales, E. Norman, P. Negri, A. Nucciotti, M. Pedretti, C. Pobes, V. Palmieri, M. Pavan, G. Pessina, S. Pirro, E. Previtali, C. Rosenfeld, A. Smith, M. Sisti, G. Ventura, M. Vanzini, and L. Zanotti, Nucl. Instrum. Methods Phys. Res., Sect. A **518**, 775 (2004).
[12] J. Hartnell, J. Phys.: Conf. Series **375**, 042015 (2012).
[13] M. Redshaw, B. J. Mount, E. G. Myers, and F. T. Avignone, Phys. Rev. Lett. **102**, 212502 (2009).
[14] N. D. Scielzo, S. Caldwell, G. Savard, J. A. Clark, C. M. Deibel, J. Fallis, S. Gulick, D. Lascar, A. F. Levand, G. Li, J. Mintz, E. B. Norman, K. S. Sharma, M. Sternberg, T. Sun, and J. Van Schelt, Phys. Rev. C **80**, 025501 (2009).
[15] S. Rahaman, V.-V. Elomaa, T. Eronen, J. Hakala, A. Jokinen, A. Kankainen, J. Rissanen, J. Suhonen, C. Weber, and J. Äystö, Phys. Lett. B **703**, 412 (2011).
[16] D. A. Nesterenko, K. Blaum, M. Block, C. Droese, S. Eliseev, F. Herfurth, E. Minaya Ramirez, Yu. N. Novikov, L. Schweikhard, V. M. Shabaev, M. V. Smirnov, I. I. Tupitsyn, K. Zuber, and N. A. Zubova, Phys. Rev. C **86**, 044313 (2012).
[17] D. W. Bardayan, M. T. F. da Cruz, M. M. Hindi, A. F. Barghouty, Y. D. Chan, A. Garcia, R.-M. Larimer, K. T. Lesko, E. B. Norman, D. F. Rossi, F. E. Wietfeldt, and I. Zlimen, Phys. Rev. C **55**, 820 (1997).
[18] E. Norman, A. Smith, A. Barghouty, R. Haight, and S. Wender, Nucl. Phys. B, Proc. Suppl. **143**, 508 (2005).
[19] A. F. Barghouty, C. Brofferio, and S. Capelli, Nucl. Instrum. Methods Phys. Res., Sect. B **295**, 16 (2013).
[20] D. Hansmann, Ph.D. thesis, Gottfried Wilhelm Leibniz Universitat Hannover, 2010.
[21] N. Otuka, E. Dupont, V. Semkova, B. Pritychenko, A. Blokhin, M. Aikawa, S. Babykina, M. Bossant, G. Chen, S. Dunaeva, R. Forrest, T. Fukahori, N. Furutachi, S. Ganesan, Z. Ge, O. Gritzay, M. Herman, S. Hlavač, K. Kat, B. Lalremruata, Y. Lee, A. Makinaga, K. Matsumoto, M. Mikhaylyukova, G. Pikulina, V. Pronyaev, A. Saxena, O. Schwerer, S. Simakov, N. Soppera, R. Suzuki, S. Takács, X. Tao, S. Taova, F. Tárkányi, V. Varlamov, J. Wang, S. Yang, V. Zerkin, and Y. Zhuang, Nucl. Data Sheets **120**, 272 (2014).
[22] R. Silberberg and C. H. Tsao, Astrophys. J. Suppl. **25**, 315 (1973).
[23] R. Silberberg and C. H. Tsao, Astrophys. J. Suppl. **25**, 335 (1973).
[24] R. Silberberg, C. H. Tsao, and A. F. Barghouty, Astrophys. J. **501**, 911 (1998).
[25] J. Back and Y. Ramachers, Nucl. Instrum. Methods Phys. Res., Sect. A **586**, 286 (2008).
[26] S. G. Mashnik, A. J. Sierk, K. K. Gudima, and M. I. Baznat, J. Phys.: Conf. Series **41**, 340 (2006).
[27] M. Blann, Phys. Rev. C **54**, 1341 (1996).
[28] S. Agostinelli, J. Allison, K. Amako, J. Apostolakis, H. Araujo, P. Arce, M. Asai, D. Axen, S. Banerjee, G. Barrand, F. Behner, L. Bellagamba, J. Boudreau, L. Broglia, A. Brunengo, H. Burkhardt, S. Chauvie, J. Chuma, R. Chytracek, G. Cooperman, G. Cosmo, P. Degtyarenko, A. Dell'Acqua, G. Depaola, D. Dietrich, R. Enami, A. Feliciello, C. Ferguson, H. Fesefeldt, G. Folger, F. Foppiano, A. Forti, S. Garelli, S. Giani, R. Giannitrapani, D. Gibin, J. Gómez Cadenas, I. González, G. Gracia Abril, G. Greeniaus, W. Greiner, V. Grichine, A. Grossheim, S. Guatelli, P. Gumplinger, R. Hamatsu, K. Hashimoto, H. Hasui, A. Heikkinen, A. Howard, V. Ivanchenko, A. Johnson, F. Jones, J. Kallenbach, N. Kanaya, M. Kawabata, Y. Kawabata, M. Kawaguti, S. Kelner, P. Kent, A. Kimura, T. Kodama, R. Kokoulin, M. Kossov, H. Kurashige, E. Lamanna, T. Lampén, V. Lara, V. Lefebure, F. Lei, M. Liendl, W. Lockman, F. Longo, S. Magni, M. Maire, E. Medernach, K. Minamimoto, P. Mora de Freitas, Y. Morita, K. Murakami, M. Nagamatu, R. Nartallo, P. Nieminen, T. Nishimura, K. Ohtsubo, M. Okamura, S. O'Neale, Y. Oohata, K. Paech, J. Perl, A. Pfeiffer, M. Pia, F. Ranjard, A. Rybin, S. Sadilov, E. Di Salvo, G. Santin, T. Sasaki, N. Savvas, Y. Sawada, S. Scherer, S. Sei, V. Sirotenko, D. Smith, N. Starkov, H. Stoecker, J. Sulkimo, M. Takahata, S. Tanaka, E. Tcherniaev, E. Safai Tehrani, M. Tropeano, P. Truscott, H. Uno, L. Urban, P. Urban, M. Verderi, A. Walkden, W. Wander, H. Weber, J. Wellisch, T. Wenaus, D. Williams, D. Wright, T. Yamada, H. Yoshida, and D. Zschiesche, Nucl. Instrum. Methods Phys. Res. Sect. A **506**, 250 (2003).
[29] J. Allison, K. Amako, J. Apostolakis, H. Araujo, P. A. Dubois, M. Asai, G. Barrand, R. Capra, S. Chauvie, R. Chytracek, G. A. P. Cirrone, G. Cooperman, G. Cosmo, G. Cuttone, G. G. Daquino, M. Donszelmann, M. Dressel, G. Folger, F. Foppiano, J. Generowicz, V. Grichine, S. Guatelli, P. Gumplinger, A. Heikkinen, I. Hrivnacova, A. Howard, S. Incerti, V. Ivanchenko, T. Johnson, F. Jones, T. Koi, R. Kokoulin, M. Kossov, H. Kurashige, V. Lara, S. Larsson, F. Lei, O. Link, F. Longo, M. Maire, A. Mantero, B. Mascialino, I. Mclaren, P. M. Lorenzo, K. Minamimoto, K. Murakami, P. Nieminen, L. Pandola, S. Parlati, L. Peralta, J. Perl, A. Pfeiffer, M. G. Pia, A. Ribon, P. Rodrigues, G. Russo, S. Sadilov, G. Santin, T. Sasaki, D. Smith, N. Starkov, S. Tanaka, E. Tcherniaev, B. Tomé, A. Trindade, P. Truscott, L. Urban, M. Verderi, A. Walkden, J. P. Wellisch, D. C. Williams, D. Wright, and H. Yoshida, IEEE Trans. Nucl. Sci. **53**, 270 (2006).
[30] http://wnr.lanl.gov.
[31] M. Gordon, P. Goldhagen, K. Rodbell, T. Zabel, H. Tang, J. Clem, and P. Bailey, IEEE Trans. Nucl. Sci. **51**, 3427 (2004).
[32] S. A. Wender, S. Balestrini, A. Brown, R. Haight, C. Laymon, T. Lee, P. Lisowski, W. McCorkle, R. Nelson, W. Parker, and N. Hill, Nucl. Instrum. Methods Phys. Res. A **336**, 226 (1993).
[33] B. S. Wang, Ph.D. thesis, University of California, Berkeley, 2014.
[34] K. J. Thomas, A. R. Smith, Y. D. Chan, E. B. Norman, B. S. Wang, and D. L. Hurley, AIP Conf. Proceed. **1549**, 20 (2013).
[35] http://lbf.lbl.gov.

[36] M. C. Perillo Isaac, D. Hurley, R. J. McDonald, E. B. Norman, and A. R. Smith, Nucl. Instrum. Methods Phys. Res. A **397**, 310 (1997).
[37] J. Boson, G. Ågren, and L. Johansson, Nucl. Instrum. Methods Phys. Res. Sect. A **587**, 304 (2008).
[38] N. Huy, D. Binh, and V. An, Nucl. Instrum. Methods Phys. Res. Sec. A **573**, 384 (2007).
[39] R. Helmer, J. Hardy, V. Iacob, M. Sanchez-Vega, R. Neilson, and J. Nelson, Nucl. Instrum. Methods Phys. Res. Sect. A **511**, 360 (2003).
[40] Z. Wang, B. Kahn, and J. Valentine, IEEE Trans. Nucl. Sci. **49**, 1925 (2002).
[41] R. R. Kinsey, C. L. Dunford, J. K. Tuli, and T. W. Burrows, *Ninth International Symposium of Capture-Gamma-Ray Spectroscopy and Related Topics* (Springer Hungarica Ltd., Budapest, 1997), p. 657.
[42] F. Alessandria *et al.*, arXiv:1109.0494.
[43] B. Quiter, Masters thesis, University of California, Berkeley, 2005.